Asian Journal of Chemistry; Vol. 37, No. 5 (2025), 1090-1100

ASIAN JOURNAL OF CHEMISTRY

https://doi.org/10.14233/ajchem.2025.33563

Synthesis, Crystal Structure and DFT Analysis of 2-(2-Chlorophenyl)-1*H*-benzo[*d*]imidazole as Charge Transport and Non-Linear Optical Material

PETER SOLO[1,2,*], DZIESEKHRIETUO KHRUOMO[3], ANTIDONG JAMIR[3], VESTAL SANKHRO[1], VESÜTOLÜ SWÜRO[1], NÜKÜTHO KHÜSOH[1] and NILO KATTI[1]

[1]Department of Chemistry, St. Joseph's College (A) Jakhama, Kohima-797001, India
[2]Department of Environmental Studies, St. Xavier College, Jalukie-797110, India
[3]Department of Physics, St. Joseph's College (A) Jakhama, Kohima-797001, India

*Corresponding author: E-mail: solopeter82@gmail.com

Received: 24 February 2025; *Accepted*: 24 March 2025; *Published online*: 30 April 2025; AJC-21974

A benzimidazole crystal, specifically 2-(2-chlorophenyl)-1*H*-benzo[*d*]imidazole, exhibiting distinctive unit cell parameters has been synthesized and its crystal structure (CCDC no: 2390665) has been confirmed through single-crystal X-ray diffraction. The stability of the structure is primarily attributed to N-H---N interactions, while relatively weaker Cl---H interactions also play a role in the crystal formation. Hirshfeld surface analysis has been employed to investigate the non-covalent interactions and to gain insights into the crystal packing. Additionally, DFT quantum chemical calculations have been conducted to examine reactivity indices, electronic transition band gaps and the density of states of the synthesized compound. It is postulated that this compound not only contributes to the existing crystallographic data but may also serve as a material for ambipolar charge transfer applications, as well as in optical and nonlinear optical studies.

Keywords: Benzimidazole, DFT, Hirshfeld surface, Density of states.

INTRODUCTION

Heterocyclic compounds have emerged as very versatile compounds with application in numerous fields like, medicine [1,2], agrochemistry [3], polymers [4], organic electronics [5] and other areas. Imidazole is a 5-membered heterocyclic compound with two annular nitrogen with the formula $C_3N_2H_4$. The ring is amphoteric due to the presence of pyrrole-like and pyridine-like nitrogen in the ring and are susceptible to the electrophilic and nucleophilic attack [6]. Benzimidazole is a bicyclic hetero-aromatic compound with a fused benzene and imidazole compound. Benzimidazoles are commonly prepared by the condensation of *o*-phenylenediamines with carboxylic compounds [7] or aldehydes [8].

The benzimidazole nucleus forms a constituent of vitamin B_{12} and other cobamides [9-11]. Benzimidazole compounds are found to exhibit pharmacological activities such as antituberculosis [12], antitumor [13], antimalarial [14], antihistamine [15], antidiabetic [16], antimicrobial [17], antiviral [18,19], anticancer [17,20], anti-inflammatory [21,22], antioxidants [21], analgetics [22], anti-HIV [23], *etc*. Besides their biological activity they have found applications in organic light emitting diodes (OLEDs) [24,25], chemosensors [26], fluorescent [27] and phosphorescent materials [28], solar cells [29], corrosion inhibitors [30], non-linear optical (NLO) materials [31,32], *etc*. In this work, a substituted benzimidazole molecule with different unit cell parameters is reported with respect to already existing structure and the crystal structure has been examined extensively. DFT studies have also been performed to study its charge transport properties, NLO properties, band gap, density of states (DOS) and excitation properties.

EXPERIMENTAL

The chemicals and solvents were obtained from different commercial suppliers and used as provided. The FT-IR spectra of the compound were examined within the range of 4000-400 cm^{-1} utilizing a Bruker FTIR ALPHA instrument with KBr in

pellet form. Additionally, the UV-visible spectrum of the compound was obtained using a Shimadzu UV-1800 UV-visible spectrophotometer, employing ethanol as solvent.

Synthesis: The synthesis of 2-(2-chlorophenyl)-1*H*-benzo-[*d*]imidazole was achieved through a one-pot condensation reaction involving *o*-phenylenediamine, 2-chlorobenzaldehyde and ammonium chloride in ethanol. The progress of the reaction was monitored by thin-layer chromatography (TLC) using a solvent system of hexane and ethyl acetate in a 1:1 ratio. Upon completion, the reaction mixture was transferred into ice-cold water, allowing for the collection of precipitates, which were subsequently purified *via* recrystallization in ethanol. Crystals of 2-(2-chlorophenyl)-1*H*-benzo[*d*]imidazole were successfully obtained through a slow-evaporation technique in ethanol (**Scheme-I**).

Single crystal X-ray diffraction analysis: Single crystal X-ray diffraction analysis was conducted utilizing a BRUKER APEX-II CCD diffractometer, employing graphite-monochromated Mo*K*α radiation (K = 0.71073 Å) at 296.15 K. The resulting diffraction data were processed through the Olex2 graphical user interface [33]. The structure was determined using direct methods with the SHELXS-08 software, while refinement was carried out using full matrix least squares with the SHELXL-2008 program [34,35]. Subsequently, the crystallographic information file was submitted to the Cambridge Crystallographic Data Centre (CCDC).

Computational analyses: The computational analyses were performed on a workstation featuring an Intel i9, 12th Generation processor with 24 cores. DFT studies were carried out using the Gaussian 09 program [36]. The analysis of hydrogen bonds and the molecular electrostatic potential (MEP) was conducted based on the optimized output structure obtained from Gaussian optimizations. Gas phase optimization calculations utilized the DFT(B3LYP) method with 6-311g++(d,p) basis sets. All constrained optimizations were executed using the DFT(B3LYP) method with 6-31g basis sets, where polarization and diffusion functions were excluded to reduce computational time. In the process of constrained optimization, all surrounding molecules are fixed, allowing the optimization to focus solely on the molecules of interest. The calculations employing TD-DFT were carried out with the X3LYP functional and the 6-31++G(d,p) basis set. SMD was utilized as the solvent model, with ethanol designated as the solvent, as reported by Kostjukova *et al*. [37]. The output files from the DFT gas-phase optimization served as the basis for the analysis of molecular reactivity indices. From the computed values of the HOMO and LUMO orbitals, energy gap (ΔE_{GAP}), ionization potential (I), electron affinity (A), electronic chemical potential (μ), electronegativity (χ), chemical hardness (η), chemical softness (S), electrophilicity index (ω) and dipole moment were derived. The parameters were calculated using the following equations [38]:

Ionization potential (I):

$$I = -E_{HOMO} \quad (1)$$

Electron affinity (A):

$$A = -E_{LUMO} \quad (2)$$

Electronic chemical potential (μ):

$$\mu = \frac{E_{HOMO} + E_{LUMO}}{2} = -\frac{I + A}{2} \quad (3)$$

Electronegativity (χ):

$$\chi = -\mu = \frac{I + A}{2} \quad (4)$$

Chemical hardness (η):

$$\eta = \frac{E_{LUMO} - E_{HOMO}}{2} = \frac{I - A}{2} \quad (5)$$

Chemical softness (S):

$$S = \frac{1}{\eta} \quad (6)$$

Electrophilicity index (ω):

$$\omega = \frac{\mu^2}{2\eta} \quad (7)$$

Hyperpolarizability serves as a measure of the nonlinear optical activity of a molecule. The first molecular hyperpolarizability is calculated based on ten specific components: β_{xxx}, β_{xxy}, β_{xyy}, β_{yyy}, β_{xxz}, β_{xyz}, β_{yyz}, β_{xzz}, β_{yzz} and β_{zzz}. These components are determined through Gaussian optimization using the B3LYP functional and the 6-311++g(d,p) basis set. The equation for first order hyperpolarizability (β_{total}) is given as [39]:

$$\beta_{total} = \left(\beta_x^2 + \beta_y^2 + \beta_z^2\right)^{1/2}$$

where, $\beta_x = \beta_{xxx} + \beta_{xyy} + \beta_{xzz}$, $\beta_y = \beta_{yyy} + \beta_{xxy} + \beta_{yzz}$, $\beta_z = \beta_{zzz} + \beta_{xxz} + \beta_{yyz}$.

Band gap and DOS calculations were performed using DFT with the Quantum Espresso package [40]. 200 atoms were considered in the unit cell and k-points were calibrated to 633.

Hydrogen bond analysis: The investigation of hydrogen bonding interactions was conducted utilizing Multiwfn, a software designed for the analysis of electronic wave functions. Single point energy calculations for the target structure were executed employing Gaussian DFT (B3LYP) methods with 6-311++(d,p) basis sets. CHK files were transformed into FCHK files, which were subsequently converted into WFX files for use in Multiwfn. The binding energy of the hydrogen bonds was estimated based on the electron density at the bond critical

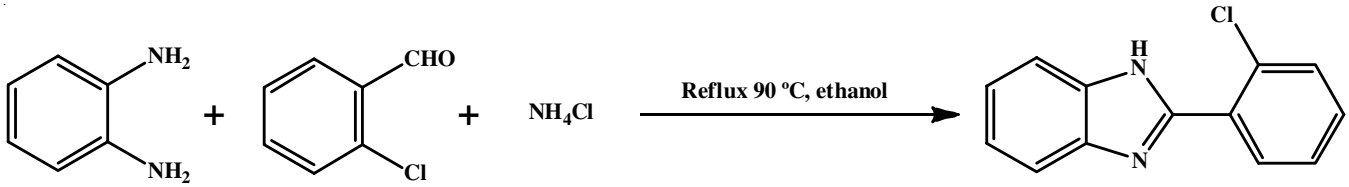

Scheme-I: Synthesis of 2-(2-chlorophenyl)-1*H*-benzo[*d*]imidazole

point (BCP) [41]. The equation for binding energy in a neutral H-bond is given as:

$$BE \approx -223.08 \times \rho(r_{BCP}) + 0.7423 \quad (8)$$

The symbol ρ (a.u.) represents the electron density at the bond critical point, while BE (kcal/mol) denotes the hydrogen binding energy.

Hirshfeld surface: The Hirshfeld surface is determined by the molecular configuration and the proximity of its nearest neighbours, thus offering valuable information about intermolecular interactions. The analysis of the Hirshfeld surface was performed using the Crystal Explorer program [42]. The 2D fingerprint plots were generated to assess all possible interactions within the crystal. In these plots, d_i indicates the distances from the Hirshfeld surface to the nearest nucleus located inside the surface, while d_e represents the distances to the nearest nucleus outside the surface. These fingerprint plots serve as a visual representation of all interatomic interactions that contribute to the overall packing of the crystal. The analysis also takes into account the reciprocal contact of each interatomic interaction. Moreover, the calculations for shape index and curvedness were also conducted for the structure.

Calculation of reorganization energy: The Marcus-Hus semi-classical model is generally utilized for the examination of charge transport characteristics in the organic materials [43]. This model posits that the rate of charge transfer in such materials is influenced by the reorganization energy resulting from geometric relaxation during the charge transfer process, as well as the electron coupling, which refers to the orbital overlap between adjacent molecules [44]. The model has been employed in the theoretical investigations of charge transport systems within the organic crystals [45-47]. The charge transfer rate (k) according to Marcus theory [48,49] may be expressed as follows:

$$k = \left(\frac{\pi}{\lambda k_b T}\right)^{1/2} \frac{V^2}{\hbar} e^{\left(-\frac{\lambda}{4k_b T}\right)}$$

where T = temperature; k_b = Boltzmann constant; V = effective intermolecular electronic coupling; λ = Reorganization energy.

The adiabatic potential energy surface method, specifically the four-point approach, is employed for the calculation of reorganization energy [43]. As illustrated in Fig. 1, Δg represents the geometric change that occurs during oxidation or reduction, while ΔE denotes the energy of adiabatic ionization. E_0^0 corresponds to the ground state of the neutral system, whereas E_0^+/E_0^- indicates the charged states resulting from oxidation or reduction. Additionally, E_+^+/E_-^- signifies the relaxed states of the oxidized or reduced species and E_+^0/E_-^0 reflects the energy of neutral state within the geometry of the oxidized or reduced configuration.

The overall reorganization energy is comprised of two components: the geometric relaxation energies (λ_h^+/λ_e^-) associated with the transition from the neutral-state geometry to the charged-state geometry and the geometric relaxation energies (λ_h^0/λ_e^0) related to the transition from the charged-state geometry back to the neutral-state geometry. The hole reorganization energy (λ_h) and the electron reorganization energy (λ_e) are defined in eqns. 10 and 11:

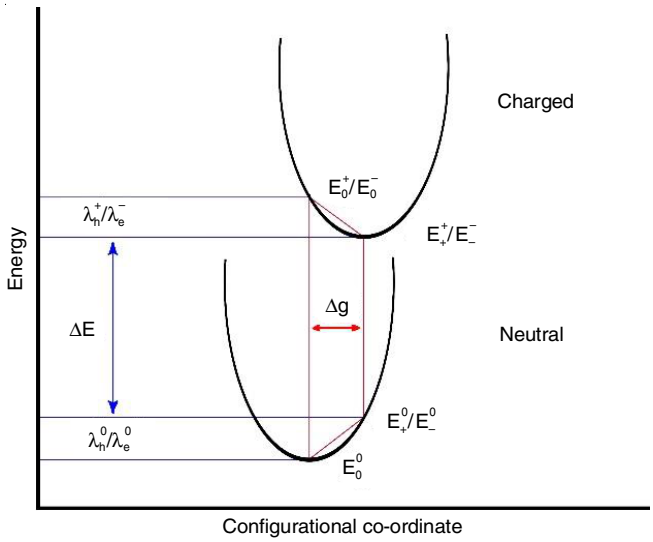

Fig. 1. Energy potential diagram for four-point approach [50]

$$\lambda_h = \lambda_h^0 + \lambda_h^+ = (E_+^0 - E_0^0) + (E_0^+ - E_+^+) \text{ (for hole transport)} \quad (10)$$

$$\lambda_e = \lambda_e^0 + \lambda_e^- = (E_-^0 - E_0^0) + (E_0^- - E_-^-) \text{ (for electron transport)} \quad (11)$$

To determine the reorganization energy, the molecules were initially optimized in their neutral state for both hole and electron reorganization energies. Subsequently, single point energy calculations were performed by either removing an electron (for hole reorganization energy) or adding an electron (for electron reorganization energy). Following this, the geometry of the molecule was optimized again after the electron was either removed or added. Finally, single point energy calculations were conducted on the optimized geometry resulting from the addition (for hole reorganization energy) or removal (for electron reorganization energy) of an electron.

RESULTS AND DISCUSSION

Brown crystalline precipitates of 2-(2-chlorophenyl)-1*H*-benzo[*d*]imidazole was recrystallized multiple times to obtain a pure form, characterized by a melting point of 232 ºC. The crystals were developed through a slow evaporation technique using ethanol. The FT-IR spectrum (Fig. 2) shows an N-H

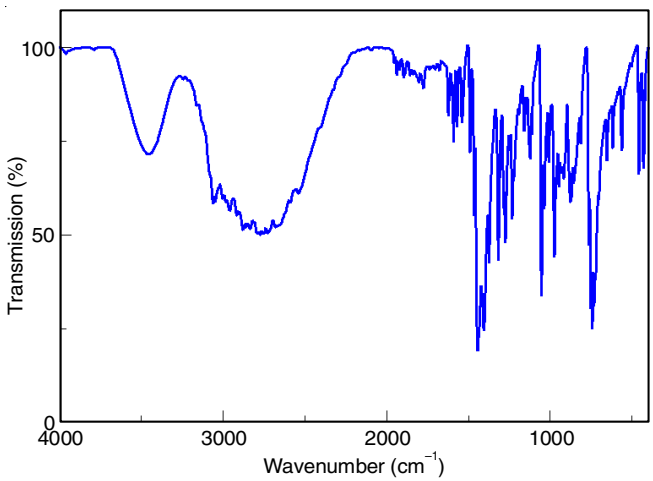

Fig. 2. FT-IR spectrum of 2-(2-chlorophenyl)-1*H*-benzo[*d*]imidazole

stretching frequency at 3453 cm^{-1} and a C-H stretching range from 2436 to 3065 cm^{-1}.

Crystal structure of 2-(2-chlorophenyl)-1*H*-benzo[*d*]-imidazole: The crystallographic details pertaining to 2-(2-chlorophenyl)-1*H*-benzo[*d*]imidazole have been archived in the Cambridge Crystallographic Data Centre, with the CCDC number 2390665 assigned to it. The database also contains three additional crystal structures of the same molecule, which are cataloged under CCDC numbers 960494 [51], 1062232 [52] and 2218513 [53]. Each of these structures presents distinct unit cell lengths, leading to variations in both volume and density. Comprehensive information on data collection, structure solution and refinement, along with the unit cell parameters of the examined compound, is provided in Table-1.

The ortep diagram of the asymmetric unit is shown in Fig. 3a. The unit cell consists of 8 molecules of 2-(2-chlorophenyl)-1*H*-benzo[*d*]imidazole and is shown in Fig. 3b.

The crystal structure depicted in Fig. 4 along the *b*-axis reveals that the benzo-imidazole rings are arranged in ribbon-like layers, forming a herringbone pattern. This structural feature

TABLE-1
CRYSTAL DATA AND STRUCTURE REFINEMENT DETAILS OF 2-(2-CHLOROPHENYL)-1*H*-BENZO[*d*]IMIDAZOLE

CCDC number	2390665
Empirical formula	$C_{13}H_9N_2Cl$
Formula weight	228.67 mol/g
Temperature	296 K
Wavelength	0.71073 Å
Crystal system	Orthorhombic
Space group	P b c a
Unit cell dimensions	a = 7.0556(13) Å; α = 90° b = 9.9612(19) Å; β = 90° c = 32.432(6) Å; γ = 90°
Cell volume	2279.4(7)
Cell formula units (Z)	8
Density	1.333 g/cm^3
F(000)	944.0
θ max for data collection	28.463°
Index ranges	$-9 \le h \le 9, -13 \le k \le 13, -43 \le l \le 43$
Data completeness	99.7%
Refinement method	Full-matrix least-squares on F^2
Goodness-of-fit on F^2	1.109

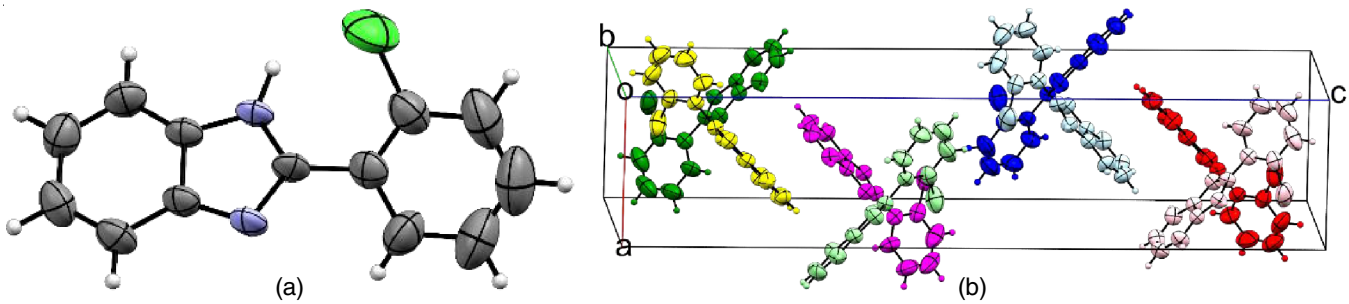

Fig. 3. Crystal structure of 2-(2-chlorophenyl)-1*H*-benzo[*d*]imidazole (a) Ortep diagram of asymmetric unit (b) Unit cell diagram (different colours representing different molecules)

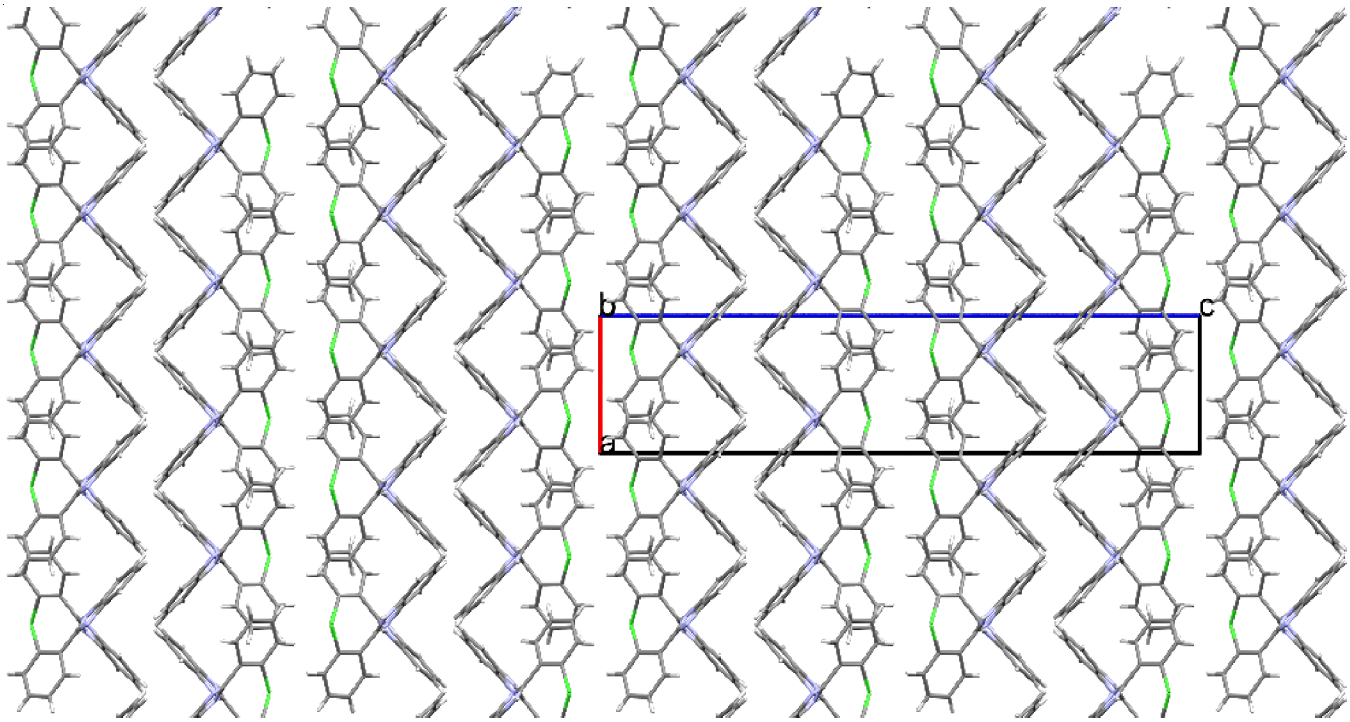

Fig. 4. Herringbone pattern of crystal arrangement along b-axis

is frequently encountered in molecular crystals that include aromatic compounds [54]. In this crystal, the molecules are bonded through N-H---N interactions, which contribute to the formation of the herringbone pattern in the ab plane.

Illustrated in Fig. 5, the N-H---N binding interaction within the crystal exhibits a distance of 1.871 Å. The electron density, $\rho(r_{BCP})$, at the bond critical point for the N-H---N bond was found to be 0.03539 a.u., while the calculated binding energy is -7.2 kcal/mol, suggesting that this interaction represents a weak hydrogen bonding scenario [55].

RMSD and R-squared analysis: In reference to the experimental XRD results, the RMSD and R-squared correlations for the gas phase and constrained phase are computed. The visual representations of the gas phase and constrained phase are displayed in Fig. 6a-b.

The computed values for RMSD and R-squared correlations are presented in Table-2, while the details regarding bond lengths, bond angles and dihedral angles are given in Tables 3-5. Both the gas phase and constrained phase exhibit minimal deviation and strong correlation concerning bond lengths and bond angles. However, a notable deviation is observed in the RMSD values for dihedral angles. Specifically, the gas phase displays an RMSD of 17.803, whereas the constrained phase shows an RMSD of 2.174. This significant deviation is primarily due to variations in the dihedrals N2-C5-C9-C16 and N3-C5-C9-C17, as detailed in Table-5. These dihedrals are associated with the bond C5-C9, which links the benzo-imidazole ring to the chloro-phenyl ring. In XRD structure, the dihedral angles N2-C5-C9-C16 and N3-C5-C9-C17 are measured at 45º and 37º, respectively, while the gas phase geometry is

TABLE-2
RESULTS OF RMSD AND R-SQUARED CORRELATION CALCULATION

		Gas phase	Constrained phase
Bond length	RMSD	0.021	0.037
	R-squared	0.991	0.972
Bond angle	RMSD	1.322	0.893
	R-squared	0.967	0.984
Dihedral angle	RMSD	17.803	2.174
	R-squared	0.989	0.993

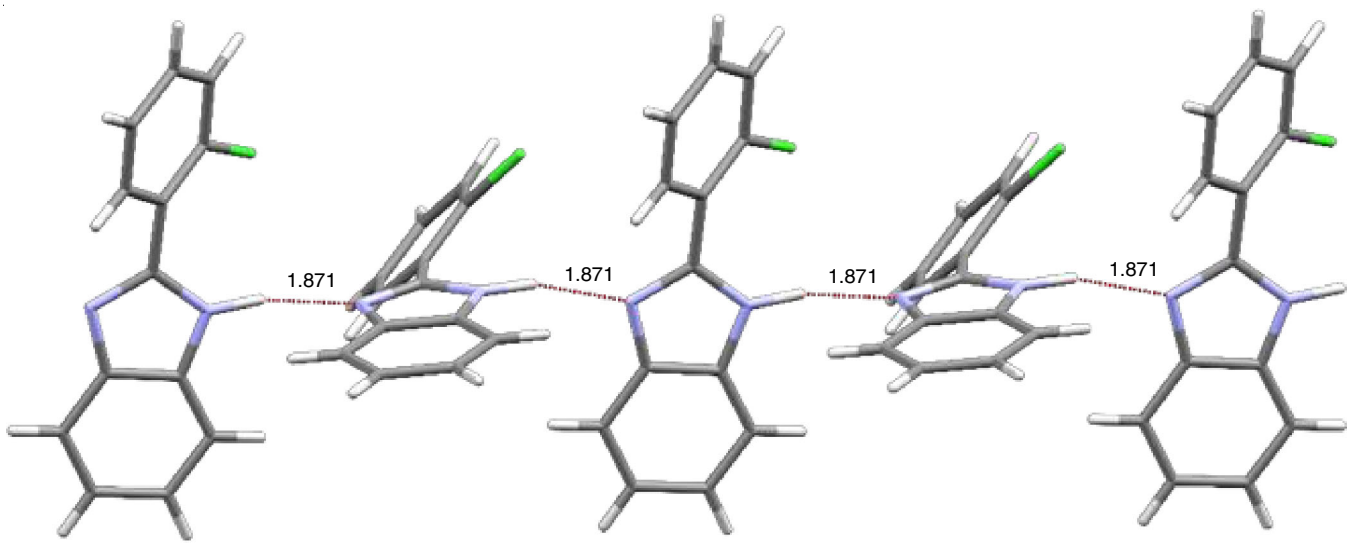

Fig. 5. Hydrogen bonding interaction in 2-(2-chlorophenyl)-1*H*-benzo[*d*]imidazole crystal

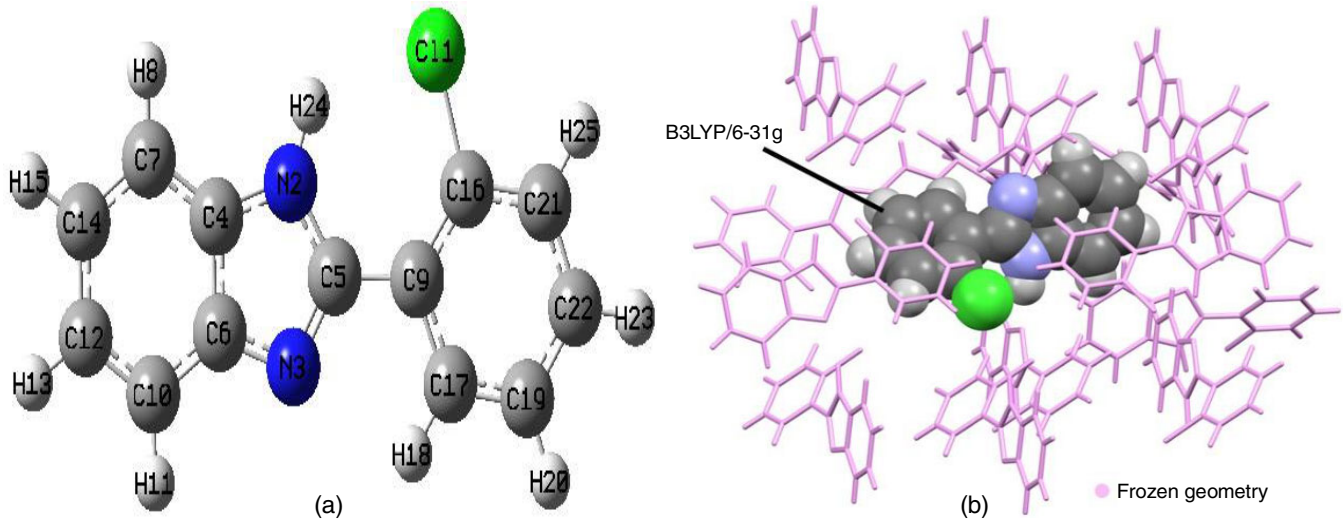

Fig. 6. Optimized structure of 2-(2-chlorophenyl)-1*H*-benzo[*d*]imidazole (a) Gas phase (b) Constrained phase

TABLE-3
BOND LENGTH COMPARISON WITH GAS PHASE AND CONSTRAIN PHASE OPTIMIZATION

Bond length	XRD	Gas phase	Constrain phase
Cl1-C16	1.72058	1.77438	1.83418
C16-C21	1.38793	1.39322	1.39095
C9-C16	1.38959	1.40515	1.40294
C5-C9	1.46718	1.47332	1.46604
N2-C5	1.35263	1.38053	1.37972
N2-H24	0.98391	1.00720	1.03352
N2-C4	1.37193	1.37895	1.38753
N3-C5	1.32547	1.31922	1.34023
N3-C6	1.37865	1.37756	1.39799
C4-C7	1.37675	1.39539	1.39972
C12-C14	1.40910	1.41001	1.41624
C6-C10	1.39071	1.40113	1.40293
C9-C17	1.38463	1.41069	1.41248
C19-C22	1.37134	1.39481	1.39905
RMSD		0.021	0.037
R-squared		0.991	0.972

TABLE-4
BOND ANGLE COMPARISON WITH GAS PHASE AND CONSTRAIN PHASE OPTIMIZATION

Bond angle	XRD	Gas phase	Constrain phase
Cl1-C16-C21	117.85391	114.99320	116.42641
Cl1-C16-C9	121.49963	123.02626	120.93179
C16-C21-C22	120.27549	120.07108	119.32757
C19-C22-C21	120.42700	119.45835	119.80175
C17-C19-C22	119.83787	119.98439	119.94427
C9-C17-C19	121.00961	122.18936	121.57117
C5-C9-C16	123.90863	127.63021	125.39256
C5-C9-C17	118.29026	116.05352	117.84083
N2-C5-C9	124.71854	125.85572	125.11833
N3-C5-C9	123.10178	122.34794	123.12946
N2-C5-N3	111.95051	111.79633	111.60884
C4-N2-C5	108.36074	107.53133	107.59159
C5-N3-C6	104.99974	105.94957	106.05715
N2-C4-C6	104.31777	104.66297	105.65868
N3-C6-C4	110.36755	110.05980	109.08081
N2-C4-C7	132.94368	132.81077	132.25260
N3-C6-C10	130.75566	130.09833	130.43648
C4-C7-C14	117.44632	116.67709	116.84143
C6-C4-C7	122.73081	122.52625	122.08565
C4-C6-C10	118.87396	119.84187	120.48051
C6-C10-C12	118.81559	117.92453	117.56623
C10-C12-C14	121.08856	121.47348	121.53725
RMSD		1.322	0.893
R-squared		0.967	0.984

linear, resulting in both dihedrals being zero. Conversely, the constrained phase exhibits only a minor deviation from the specified dihedral angles. It can be inferred that the structure of the constrained phase demonstrates a higher correlation and reduced deviation from the experimental structure.

The transition of the dihedral angle N2-C5-C9-C16 from the gas phase to the crystalline phase is shown in Fig. 7, highlighting the associated energy barrier. In the crystalline phase, the dihedral angle is -45.14º, contrasting with -0.05º in the gas phase. The calculated energy required for rotation about the C5-C9 bond is roughly 1.004 kcal/mol.

Molecular reactivity indices analysis: The parameters related to the reactivity indices of 2-(2-chlorophenyl)-1*H*-benzo[*d*]imidazole are detailed in Table-6. The electronic chemical potential (μ) value, which reflects the system's capacity to exchange electron density with its environment at the ground state, indicates a slight electron-donor character for the molecule [38]. The values of electronegativity characterize the molecule as having low electronegativity. Chemical hardness (η), which denotes the resistance of a molecule to the exchange of electron density with its surroundings, is low for this compound, suggesting a stable ground state structure [38]. The electrophilicity index (ω), which assesses the energy stabilization of a molecule when it gains additional electron density, shows that this compound, with an electrophilicity index of 3.66, is regarded as a strong electrophile [56].

TABLE-5
DIHEDRAL COMPARISON WITH GAS PHASE AND CONSTRAIN PHASE OPTIMIZATION

Dihedral angle	XRD	Gas phase	Constrain phase
Cl1-C16-C9-C5	-0.48092	-0.00051	3.85786
N2-C5-C9-C16	45.14529	-0.05568	40.24253
N3-C5-C9-C17	37.88356	-0.04566	35.22549
C9-C16-C21-C22	-0.52824	0.00141	-0.67830
C17-C19-C22-C21	-0.40089	-0.00113	0.70042
C16-C9-C17-C19	-1.52138	-0.00164	-0.71274
N2-C4-C6-N3	-0.47363	-0.00365	-0.54215
N3-C5-N2-C4	-0.56234	-0.00467	-0.31090
C6-C4-C7-C14	0.29382	-0.00346	0.00105
C7-C14-C12-C10	0.09262	0.00000	0.22942
C4-C6-C10-C12	0.95460	0.00039	1.00903
RMSD		17.803	2.174
R-squared		0.989	0.993

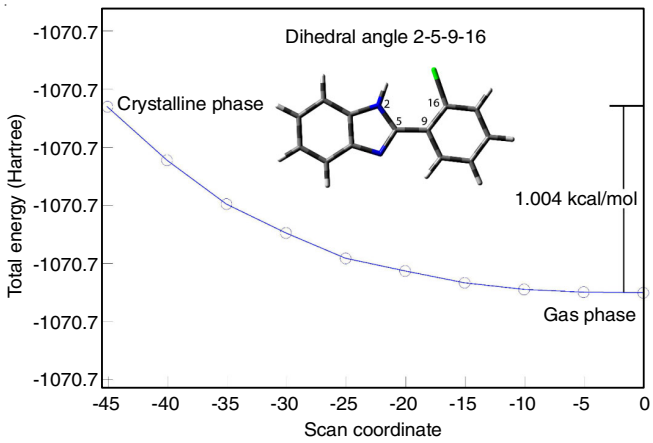

Fig. 7. Calculated energy-change in dihedral angle N2-C5-C9-C16

TABLE-6
MOLECULAR REACTIVITY INDICES ANALYSIS FOR 2-(2-CHLOROPHENYL)-1*H*-BENZO[*d*]IMIDAZOLE

Quantum chemical descriptors	(eV)
Ionization potential (I) = $-E_{HOMO}$	6.16
Electron affinity (A) = $-E_{LUMO}$	1.81
ΔE_{gap}	4.35
Electronic chemical potential (μ)	-3.99
Electronegativity (χ)	3.99
Chemical hardness (η)	2.16
Chemical softness (S)	0.46
Electrophilicity index (ω)	3.66

Molecular electrostatic potential: In the MEP surface of studied compound under investigation (Fig. 8), the vicinity of H24 is positively charged, in contrast to the negatively charged areas surrounding N3. Thus, the compound exhibits both electrophilic and nucleophilic properties.

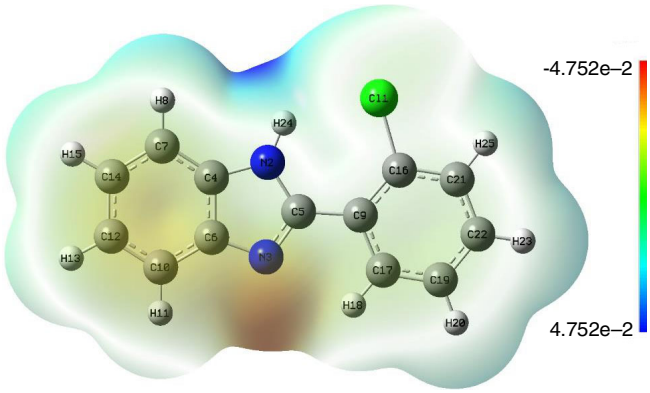

Fig. 8. MEP plot of 2-(2-chlorophenyl)-1*H*-benzo[*d*]imidazole

Hirshfeld surface of 2-(2-chlorophenyl)-1*H*-benzo[*d*]-imidazole crystal: The analysis of Hirshfeld surfaces facilitates the quantification of intermolecular interactions in crystalline systems. Figs. 9 and 10 illustrate the Hirshfeld surfaces, which include d_{norm}, shape index and curvedness. The dark red areas observed in the d_{norm} (Fig. 9) confirm the existence of hydrogen bonding interactions involving the imidazole ring and two adjacent molecules. The blue regions further indicate significant van der Waals interactions. The shape index (Fig. 10) highlights notable hollows (red regions) at both the top and bottom of the molecule, suggesting a close molecular arrangement with neighboring molecules. The lack of extensive green regions in the curvedness surface (Fig. 10) corresponds to the absence of molecular stacking among the molecules.

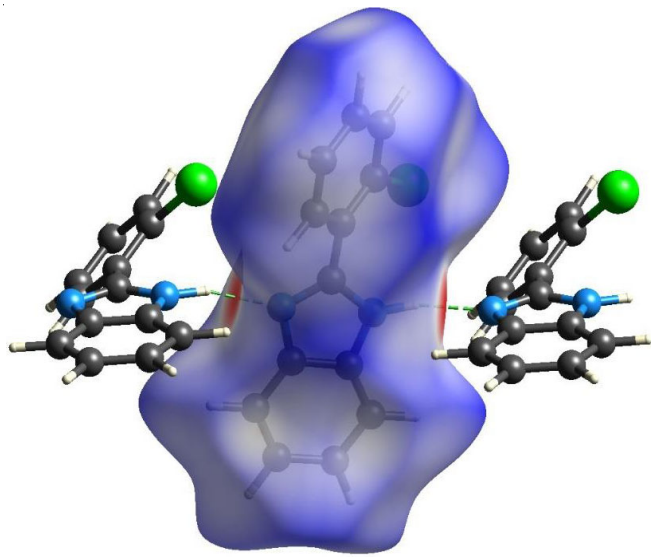

Fig. 9. Hirshfeld surface (d_{norm}) of 2-(2-chlorophenyl)-1*H*-benzo[*d*]imidazole crystal with hydrogen bonds

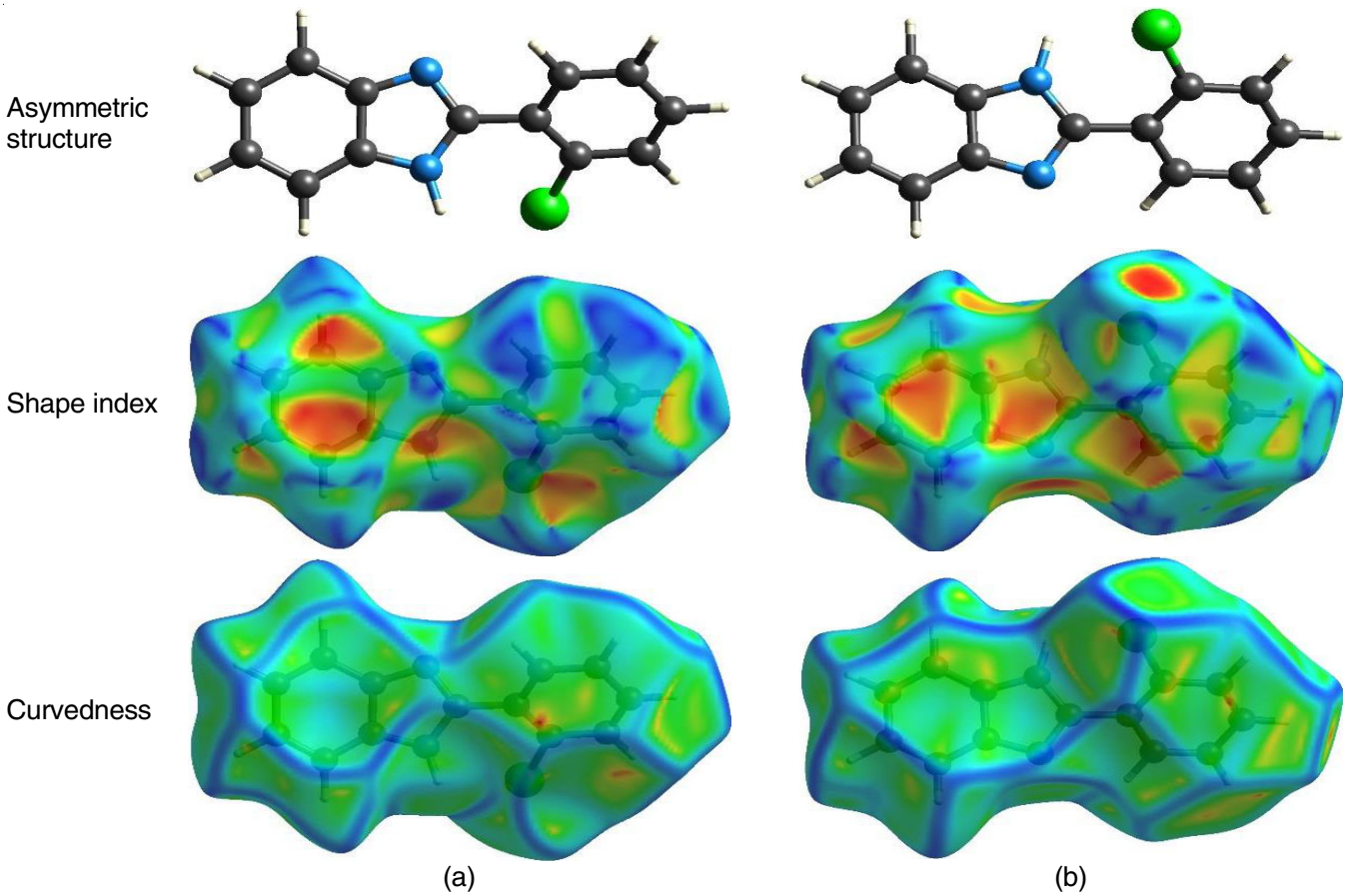

Fig. 10. Hirshfeld surface of 2-(2-chlorophenyl)-1*H*-benzo[*d*]imidazole crystal (a) Top view (b) Bottom view

The fingerprint plot for the crystal is illustrated in Fig. 11, indicating that 67% of the interactions are linked to H---H and C---H interactions. The presence of a pair of spikes at lower d_i and d_e values points to significant intermolecular N-H---N hydrogen bonds. This dual spike pattern implies that the molecule serves as both an acceptor and a donor in these interactions. Moreover, the absence of a red region in the central area of the plot suggests that π---π interactions are not present. The pair of spikes at elevated d_i and d_e values corresponds to Cl---H interactions.

Charge transport analysis: According to the principles of Marcus theory, the charge transfer rate (k) is primarily determined by the reorganization energy values. Specifically, a reduction in reorganization energy leads to an enhancement in the charge transfer rate. The computed values for hole reorganization energy ($\lambda_h = 0.34$ eV) and electron reorganization energy ($\lambda_e = 0.35$ eV) indicate that this molecule can function effectively as an ambipolar material for charge transport, given that the reorganization energies for both types of charge carriers are almost equal.

NLO analysis: Table-7 provides the values for the components of the first molecular hyperpolarizability, presented in atomic units. The computed first molecular hyperpolarizability (β_{total}) is 0.37005×10^{-30} esu, which is nearly twice that of urea's first hyperpolarizability (0.1947×10^{-30}), utilized as a reference for investigating the nonlinear optical properties of molecular

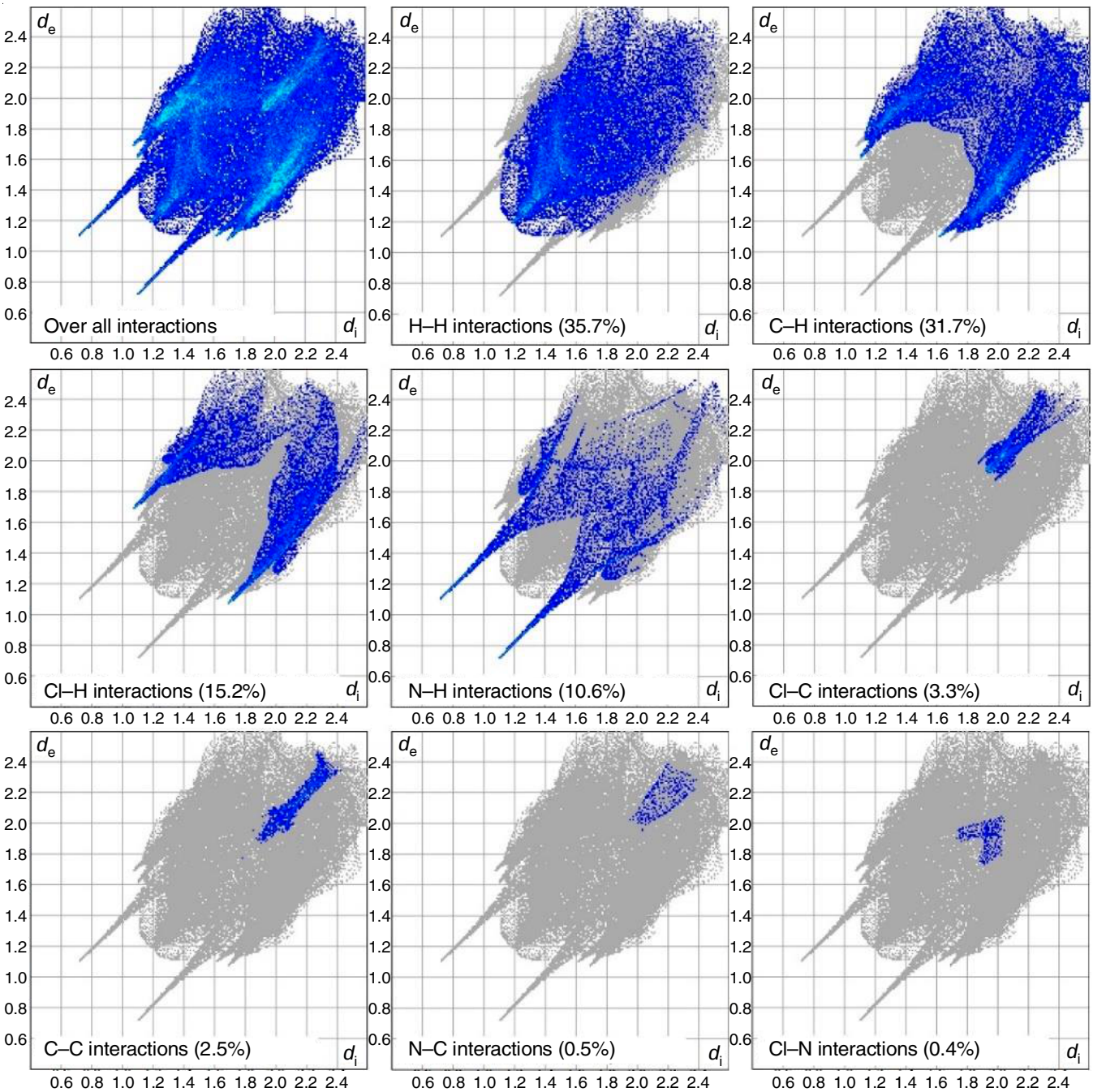

Fig. 11. Finger print plot of 2-(2-chlorophenyl)-1*H*-benzo[*d*]imidazole crystal

TABLE-7
COMPONENTS OF FIRST HYPERPOLARIZABILITY VALUES OF 2-(2-CHLOROPHENYL)-1*H*-BENZO[*d*]IMIDAZOLE

Parameters	B3LYP, 6-311++g(d,p)	Parameters	B3LYP, 6-311++g(d,p)
β_{xxx}	-35.1701	β_{yzz}	6.5731
β_{yyy}	11.6788	β_{yyz}	-0.0100
β_{zzz}	0.0044	β_{xyz}	-0.0181
β_{xyy}	-0.0799	β_{x}	1760.037428
β_{xxy}	-9.6077	β_{y}	74.72219364
β_{xxz}	0.0037	β_{z}	0.00000361
β_{xzz}	-6.7028	β_{total}	0.37005×10^{-30} esu

structures. The significant first hyperpolarizability of this molecule indicates its promising application in optoelectronic technologies.

TDOS and PDOS of 2-(2-chlorophenyl)-1*H*-benzo[*d*]-imidazole crystal: The total density of states (TDOS) serves as an indicator of the number of permissible states at specific energy levels, whereas the partial density of states (PDOS) illustrates the contribution of individual fragments or atoms to the overall density of states. Fig. 12 presents the density of states diagram, with the *x*-axis denoting energy levels in electron volts (eV) and the *y*-axis indicating the number of states per energy level. The highest occupied molecular orbital (HOMO) at 0.7421 eV and the lowest unoccupied molecular orbital (LUMO) at 4.0742 eV are marked in the diagram, revealing a band gap of 3.3321 eV. The DOS plot indicates a significant electronic transition from HOMO to LUMO, which will be further validated through UV-Vis spectroscopic analysis.

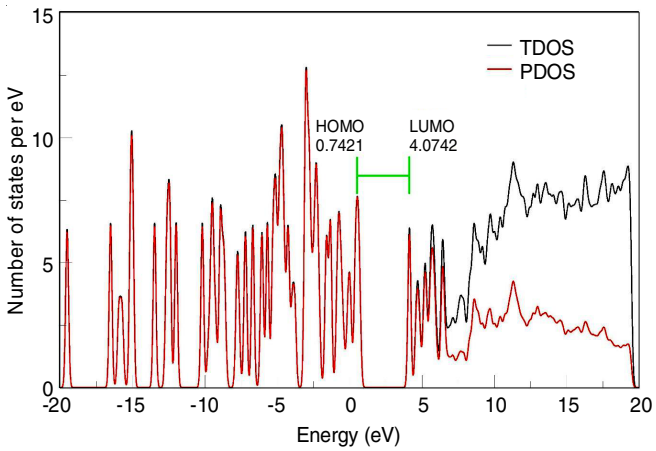

Fig. 12. Graphical representation of the TDOS and PDOS

UV-Visible studies: The UV-visible spectrum of the molecule, encompassing both experimental and theoretical data, is presented in Fig. 13. The theoretical calculations indicate that the maximum wavelength (λ_{max}) is predicted to occur at 308.89 nm, which closely aligns with the experimental measurement of 306 nm. Furthermore, the transition observed at 306 nm

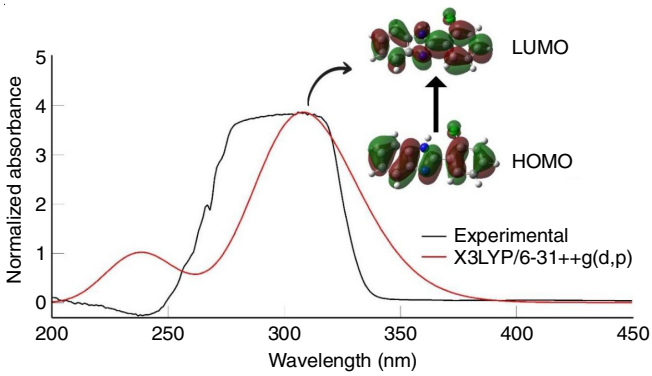

Fig. 13. UV-visible spectrum of 2-(2-chlorophenyl)-1*H*-benzo[*d*]imidazole (experimental and theoretical)

can be ascribed to the HOMO-to-LUMO transition, as suggested by the theoretical predictions.

The details of the major electronic transition are compared and outlined in Table-8. Upon analyzing the frontier molecular orbitals, it is observed that the charges are evenly distributed across the molecular surface in both the highest occupied molecular orbital and the lowest unoccupied molecular orbital.

Conclusion

A distinctive benzimidazole derivative featuring unique unit cell parameters has been synthesized, with its structure analyzed using FT-IR and single-crystal X-ray diffraction techniques. The crystal structure is primarily influenced by N-H---N hydrogen bonding, exhibiting a binding energy of -7.2 kcal/mol, which results in a herringbone arrangement within the ab plane. The stability of the crystal structure is further enhanced by Cl---H interactions. Analysis of RMSD and R-squared correlation indicates that the constrained optimized structure aligns more closely with the XRD structure, particularly regarding the angle between the benzimidazole and phenyl ring. Quantum chemical descriptors affirm the compound's stability, while MEP analysis indicates its amphoteric characteristics. Examination of the Hirshfeld surface provides insights into the crystal packing patterns and the roles of various intermolecular interactions. The first hyperpolarizability of the compound is approximately twice that of urea, suggesting its potential application as a nonlinear optical (NLO) material. Additionally, both experimental and theoretical UV-spectroscopic analyses, along with density of states studies, reveal that the electronic transition at 306 nm is predominantly a HOMO to LUMO transition. Reorganization analysis supports the recommendation of this compound as an ambipolar charge transport system.

ACKNOWLEDGEMENTS

The authors are grateful to St. Joseph's College (A) Jakhama, India for providing all the facilities to perform the study. The authors are also grateful to Sophisticated Analytical Instrumen-

TABLE-8
MAJOR ELECTRONIC TRANSITIONS OF 2-(2-CHLOROPHENYL)-1*H*-BENZO[*d*]IMIDAZOLE

Transition energy (eV)	λ (nm)	Oscillator frequency (*f*)	λ (nm) Exp.	Major orbital contribution
4.0138	308.9	0.8290	306.0	HOMO→LUMO (69.82%)

tation Centre (SAIC), Tezpur University, for the high-quality single crystal XRD data collection.

CONFLICT OF INTEREST

The authors declare that there is no conflict of interests regarding the publication of this article.

REFERENCES

1. E. Kabir and M. Uzzaman, *Results Chem.*, **4**, 100606 (2022); https://doi.org/10.1016/j.rechem.2022.100606
2. F. Ullah, S. Ullah, M.F.A. Khan, M. Mustaqeem and R.N. Paracha, *Molecules*, **27**, 6631 (2022); https://doi.org/10.3390/molecules27196631
3. C. Lamberth, *Pest Manag. Sci.*, **69**, 1106 (2013); https://doi.org/10.1002/ps.3615
4. R. Murugan, *Progr. Heterocycl. Chem.*, **35**, 93 (2023); https://doi.org/10.1016/B978-0-443-21936-8.00002-1
5. H.K. Mehta, S.K. Pathan and S.M. Trivedi, *Russ. J. Org. Chem.*, **59(S1)**, S123 (2023); https://doi.org/10.1134/S10704280231301434
6. A. Richaud, N. Barba-Behrens and F. Méndez, *Org. Lett.*, **13**, 972 (2011); https://doi.org/10.1021/ol103011h
7. R. Dubey and N.S.H. Narayana Moorthy, *Chem. Pharm. Bull.*, **55**, 115 (2007); https://doi.org/10.1248/cpb.55.115
8. Z. Wang, T. Song and Y. Yang, *Synlett*, **30**, 319 (2019); https://doi.org/10.1055/s-0037-1610353
9. B. Schulze, B. Vogler and P. Renz, *Eur. J. Biochem.*, **254**, 620 (1998); https://doi.org/10.1046/j.1432-1327.1998.2540620.x
10. S.S. Epstein, *Nature*, **188**, 143 (1960); https://doi.org/10.1038/188143a0
11. Salahuddin, M. Shaharyar and A. Mazumder, *Arab. J. Chem.*, **10**, S157 (2017); https://doi.org/10.1016/j.arabjc.2012.07.017
12. G. Sindhu, R. Kholiya, S. Kidwai, P. Singh, R. Singh and D.S. Rawat, *J. Biochem. Mol. Toxicol.*, **36**, e23123 (2022); https://doi.org/10.1002/jbt.23123
13. D.-S. Son, E.-S. Lee and S.E. Adunyah, *Immune Netw.*, **20**, e29 (2020); https://doi.org/10.4110/in.2020.20.e29
14. N. Escala, L.M. Pineda, M.G. Ng, L.M. Coronado, C. Spadafora and E. del Olmo, *Sci. Rep.*, **13**, 285 (2023); https://doi.org/10.1038/s41598-022-27351-z
15. M.S. Vasava, M.N. Bhoi, S.K. Rathwa, D.J. Jethava, P.T. Acharya, D.B. Patel and H.D. Patel, *Mini Rev. Med. Chem.*, **20**, 532 (2020); https://doi.org/10.2174/1389557519666191122125453
16. R.V. Shingalapur, K.M. Hosamani, R.S. Keri and M.H. Hugar, *Eur. J. Med. Chem.*, **45**, 1753 (2010); https://doi.org/10.1016/j.ejmech.2010.01.007
17. S.A. Patil, S.A. Patil and R. Patil, *Chem. Biol. Drug Des.*, **89**, 639 (2017); https://doi.org/10.1111/cbdd.12802
18. M. Tonelli, G. Paglietti, V. Boido, F. Sparatore, F. Marongiu, E. Marongiu, P. LaColla and R. Loddo, *Chem. Biodivers.*, **5**, 2386 (2008); https://doi.org/10.1002/cbdv.200890203
19. M. Tonelli, M. Simone, B. Tasso, F. Novelli, V. Boido, F. Sparatore, G. Paglietti, S. Pricl, G. Giliberti, S. Blois, C. Ibba, G. Sanna, R. Loddo and P. La Colla, *Bioorg. Med. Chem.*, **18**, 2937 (2010); https://doi.org/10.1016/j.bmc.2010.02.037
20. J. Nath, R. Paul, S.K. Ghosh, J. Paul, B. Singha and N. Debnath, *Life Sci.*, **258**, 118189 (2020); https://doi.org/10.1016/j.lfs.2020.118189
21. R.K. Arora, N. Kaur, Y. Bansal and G. Bansal, *Acta Pharm. Sin. B*, **4**, 368 (2014); https://doi.org/10.1016/j.apsb.2014.07.001
22. K.C.S. Achar, K.M. Hosamani and H.R. Seetharamareddy, *Eur. J. Med. Chem.*, **45**, 2048 (2010); https://doi.org/10.1016/j.ejmech.2010.01.029
23. T. Pan, X. He, B. Chen, H. Chen, G. Geng, H. Luo, H. Zhang and C. Bai, *Eur. J. Med. Chem.*, **95**, 500 (2015); https://doi.org/10.1016/j.ejmech.2015.03.050
24. R. Sathyanarayana, V. Kumar, G.H. Pujar, B. Poojary, M.K. Shankar and S. Yallappa, *J. Photochem. Photobiol. Chem.*, **401**, 112751 (2020); https://doi.org/10.1016/j.jphotochem.2020.112751
25. K. Upendranath, T. Venkatesh, Y. Arthoba Nayaka, M. Shashank and G. Nagaraju, *Inorg. Chem. Commun.*, **139**, 109354 (2022); https://doi.org/10.1016/j.inoche.2022.109354
26. P. Jana, M. Yadav, T. Kumar and S. Kanvah, *J. Photochem. Photobiol. Chem.*, **404**, 112874 (2021); https://doi.org/10.1016/j.jphotochem.2020.112874
27. H. Xu, M.-D. Lin, J. Yuan, B. Zhou, Y. Mu, Y. Huo and K. Zhu, *Chem. Commun.*, **57**, 3239 (2021); https://doi.org/10.1039/D0CC07471C
28. D. Chen, W.-Z. He, H.-S. Liao, Y.-X. Hu, D.-D. Xie, B.-Y. Wang, H.-J. Chi, Y.-L. Lv, X. Zhu and X. Li, *Org. Electron.*, **113**, 106715 (2023); https://doi.org/10.1016/j.orgel.2022.106715
29. S.A. Kuklin, S.V. Safronov, O.Yu. Fedorovskii, E.A. Khakina, L.V. Kulik, D.E. Utkin, L.A. Frolova, P.A. Troshin and A.R. Khokhlov, *Mendeleev Commun.*, **33**, 306 (2023); https://doi.org/10.1016/j.mencom.2023.04.003
30. M. Marinescu, *BMC Chem.*, **13**, 136 (2019); https://doi.org/10.1186/s13065-019-0655-y
31. S. Aslam, M. Haroon, T. Akhtar, M. Arshad, M. Khalid, Z. Shafiq, M. Imran and A. Ullah, *ACS Omega*, **7**, 31036 (2022); https://doi.org/10.1021/acsomega.2c02805
32. N. Vijayan, R. Ramesh Babu, R. Gopalakrishnan, P. Ramasamy and W.T.A. Harrison, *J. Cryst. Growth*, **262**, 490 (2004); https://doi.org/10.1016/j.jcrysgro.2003.08.082
33. O.V. Dolomanov, L.J. Bourhis, R.J. Gildea, J.A.K. Howard and H. Puschmann, *J. Appl. Cryst.*, **42**, 339 (2009); https://doi.org/10.1107/S0021889808042726
34. G.M. Sheldrick, *Acta Crystallogr. C Struct. Chem.*, **71**, 3 (2015); https://doi.org/10.1107/S2053229614024218
35. G.M. Sheldrick, *Acta Crystallogr. A*, **64**, 112 (2008); https://doi.org/10.1107/S0108767307043930
36. M.J. Frisch, G.W. Trucks, H.B. Schlegel, G.E. Scuseria, M.A. Robb, J.R. Cheeseman, G. Scalmani, V. Barone, B. Mennucci, G.A. Petersson, H. Nakatsuji, M. Caricato, X. Li, H.P. Hratchian, A.F. Izmaylov, J. Bloino, G. Zheng, J. L. Sonnenberg, M. Hada, M. Ehara, K. Toyota, R. Fukuda, J. Hasegawa, M. Ishida, T. Nakajima, Y. Honda, O. Kitao, H. Nakai, T. Vreven, J.A. Montgomery, Jr., J.E. Peralta, F. Ogliaro, M. Bearpark, J.J. Heyd, E. Brothers, K.N. Kudin, V.N. Staroverov, R. Kobayashi, J. Normand, K. Raghavachari, A. Rendell, J.C. Burant, S.S. Iyengar, J. Tomasi, M. Cossi, N. Rega, J.M. Millam, M. Klene, J.E. Knox, J.B. Cross, V. Bakken, C. Adamo, J. Jaramillo, R. Gomperts, R.E. Stratmann, O. Yazyev, A.J. Austin, R. Cammi, C. Pomelli, J.W. Ochterski, R.L. Martin, K. Morokuma, V.G. Zakrzewski, G.A. Voth, P. Salvador, J.J. Dannenberg, S. Dapprich, A.D. Daniels, Ö. Farkas, J.B. Foresman, J.V. Ortiz, J. Cioslowski, and D.J. Fox, Gaussian 09, Gaussian, Inc., Wallingford CT (2009).
37. L.O. Kostjukova, S.V. Leontieva and V.V. Kostjukov, *J. Mol. Liq.*, **336**, 116369 (2021); https://doi.org/10.1016/j.molliq.2021.116369
38. L. Domingo, M. Ríos-Gutiérrez and P. Pérez, *Molecules*, **21**, 748 (2016); https://doi.org/10.3390/molecules21060748
39. F. Mostaghni, *Acta Chim. Slov.*, **68**, 170 (2021); https://doi.org/10.17344/acsi.2020.6299
40. P. Giannozzi, S. Baroni, N. Bonini, M. Calandra, R. Car, C. Cavazzoni, D. Ceresoli, G.L. Chiarotti, M. Cococcioni, I. Dabo, A. Dal Corso, S. de Gironcoli, G. Fratesi, R. Gebauer, U. Gerstmann, C. Gougoussis, S. Fabris, A. Kokalj, M. Lazzeri, L. Martin-Samos, N. Marzari, F. Mauri, R. Mazzarello, S. Paolini, A. Pasquarello, L. Paulatto, C. Sbraccia, S. Scandolo, G. Sclauzero, A.P. Seitsonen, A. Smogunov, P. Umari and R.M. Wentzcovitch, *J. Phys. Condens. Matter*, **21**, 395502 (2009); https://doi.org/10.1088/0953-8984/21/39/395502
41. S. Emamian, T. Lu, H. Kruse and H. Emamian, *J. Comput. Chem.*, **40**, 2868 (2019); https://doi.org/10.1002/jcc.26068

42. P.R. Spackman, M.J. Turner, J.J. McKinnon, D.J. Grimwood, S.K. Wolff, D. Jayatilaka and M.A. Spackman, *J. Appl. Cryst.*, **54**, 1006 (2021); https://doi.org/10.1107/S1600576721002910
43. G.R. Hutchison, M.A. Ratner and T.J. Marks, *J. Am. Chem. Soc.*, **127**, 2339 (2005); https://doi.org/10.1021/ja0461421
44. Y.-K. Lan and C.-I. Huang, *J. Phys. Chem. B*, **112**, 14857 (2008); https://doi.org/10.1021/jp806967x
45. J.-D. Huang, K. Yu, X. Huang, D. Chen, J. Wen, S. Cheng and H. Ma, *IUCrJ*, **6**, 603 (2019); https://doi.org/10.1107/S2052252519004706
46. O. López-Estrada, H.G. Laguna, C. Barrueta-Flores and C. Amador-Bedolla, *ACS Omega*, **3**, 2130 (2018); https://doi.org/10.1021/acsomega.7b01425
47. Z. Shuai, W. Li, J. Ren, Y. Jiang and H. Geng, *J. Chem. Phys.*, **153**, 080902 (2020); https://doi.org/10.1063/5.0018312
48. R.A. Marcus, *J. Chem. Phys.*, **24**, 966 (1956); https://doi.org/10.1063/1.1742723
49. N.S. Hush, *J. Chem. Phys.*, **28**, 962 (1958); https://doi.org/10.1063/1.1744305
50. P. Solo and M.A. Doss, *J. Chem. Crystallogr.*, **54**, 183 (2024); https://doi.org/10.1007/s10870-024-01011-8
51. M. Azam, A.A. Khan, S.I. Al-Resayes, M.S. Islam, A.K. Saxena, S. Dwivedi, J. Musarrat, A. Trzesowska-Kruszynska and R. Kruszynski, *Spectrochim. Acta A Mol. Biomol. Spectrosc.*, **142**, 286 (2015); https://doi.org/10.1016/j.saa.2015.01.106
52. F. Odame, J. Krause, E.C. Hosten, R. Betz, K. Lobb, Z.R. Tshentu and C.L. Frost, *Bull. Chem. Soc. Ethiop.*, **32**, 271 (2018); https://doi.org/10.4314/bcse.v32i2.8
53. T. Boominathan and A. Sivaramakrishna, *J. Catal.*, **426**, 6 (2023); https://doi.org/10.1016/j.jcat.2023.06.041
54. A. Guijarro, J.A. Vergés, E. SanFabián, G. Chiappe and E. Louis, *ChemPhysChem*, **17**, 3548 (2016); https://doi.org/10.1002/cphc.201600586
55. T. Steiner, *Angew. Chem. Int. Ed.*, **41**, 48 (2002); https://doi.org/10.1002/1521-3773(20020104)41:1<48::AID-ANIE48>3.0.CO;2-U
56. L.R. Domingo, M.J. Aurell, P. Pérez and R. Contreras, *Tetrahedron*, **58**, 4417 (2002); https://doi.org/10.1016/S0040-4020(02)00410-6